Acta Biomaterialia 140 (2022) 233–246

Contents lists available at ScienceDirect

Acta Biomaterialia

journal homepage: www.elsevier.com/locate/actbio

Full length article

Vascular Endothelial Growth Factor-Capturing Aligned Electrospun Polycaprolactone/Gelatin Nanofibers Promote Patellar Ligament Regeneration

Zhengchao Yuan[a,1], Dandan Sheng[b,c,1], Liping Jiang[c], Muhammad Shafiq[a,d,*], Atta ur Rehman Khan[a], Rashida Hashim[e], Yujie Chen[a], Baojie Li[a], Xianrui Xie[a], Jun Chen[b], Yosry Morsi[f], Xiumei Mo[a,*], Shiyi Chen[b,*]

[a] State Key Laboratory for Modification of Chemical Fibers and Polymer Materials, Shanghai Engineering Research Center of Nano-Biomaterials and Regenerative Medicine, College of Chemistry, Chemical Engineering and Biotechnology, Donghua University, Shanghai, 201620, China
[b] Department of Sports Medicine, Huashan Hospital, Fudan University, Shanghai 200040, China
[c] State Key Laboratory of Molecular Engineering of Polymers, Department of Macromolecular Science, Fudan University, Shanghai, China
[d] Department of Biotechnology, Faculty of Life Sciences, University of Central Punjab (UCP), Lahore 54000, Pakistan
[e] Department of Chemistry, Quaid-i-Azam University (QAU), Islamabad 45320, Pakistan
[f] Faculty of Engineering and Industrial Sciences, Swinburne University of Technology, Boroondara, VIC 3122, Australia

ARTICLE INFO

Article history:
Received 20 June 2021
Revised 21 November 2021
Accepted 24 November 2021
Available online 28 November 2021

Keywords:
Electrospinning
Nanofiber
Patellar ligament
Tissue regeneration
VEGF
Peptide

ABSTRACT

Ligament injuries are common in sports and other rigorous activities. It is a great challenge to achieve ligament regeneration after an injury due the avascular structure and low self-renewal capability. Herein, we developed vascular endothelial growth factor (VEGF)-binding aligned electrospun poly(caprolactone)/gelatin (PCL/Gel) scaffolds by incorporating prominin-1-binding peptide (BP) sequence and exploited them for patellar ligament regeneration. The adsorption of BP onto scaffolds was discerned by various techniques, such as Fourier-transform infrared spectroscopy, X-ray photoelectron spectroscopy, and confocal laser scanning microscope. The accumulation of VEGF onto scaffolds correlated with the concentration of the peptide *in vitro*. BP-anchored PCL/Gel scaffolds (BP@PCL/Gel) promoted the tubular formation of human umbilical vein endothelial cells (HUVECs) and wound healing *in vitro*. Besides, BP containing scaffolds exhibited higher content of $CD31^+$ cells than that of the control scaffolds at 1 week after implantation *in vivo*. Moreover, BP containing scaffolds improved biomechanical properties and facilitated the regeneration of matured collagen in patellar ligament 4 weeks after implantation in mice. Overall, this strategy of peptide-mediated orchestration of VEGF provides an enticing platform for the ligament regeneration, which may also have broad implications for tissue repair applications.

Statement of significance

Ligament injuries are central to sports and other rigorous activities. Given to the avascular nature and poor self-healing capability of injured ligament tissues, it is a burgeoning challenge to fabricate tissue-engineered scaffolds for ligament reconstruction. Vascular endothelial growth factor (VEGF) is pivotal to the neo-vessel formation. However, the high molecular weight of VEGF as well as its short half-life *in vitro* and *in vivo* limits its therapeutic potential. To circumvent these limitations, herein, we functionalized aligned electrospun polycaprolactone/gelatin (PCL/Gel)-based scaffolds with VEGF-binding peptide (BP) and assessed their biocompatibility and performance *in vitro* and *in vivo*. BP-modified scaffolds accumulated VEGF, improved tube formation of HUVECs, and induced wound healing *in vitro*, which may have broad implications for regenerative medicine and tissue engineering.

© 2021 Acta Materialia Inc. Published by Elsevier Ltd. All rights reserved.

* Corresponding authors.
E-mail addresses: dr.muhammadshafiq@ucp.edu.pk (L. Jiang), dr.muhammadshafiq@ucp.edu.pk (M. Shafiq), xmm@dhu.edu.cn (X. Mo), cshiyi@163.com (S. Chen).
[1] These authors contributed equally to this work.

https://doi.org/10.1016/j.actbio.2021.11.040
1742-7061/© 2021 Acta Materialia Inc. Published by Elsevier Ltd. All rights reserved.

1. Introduction

Ligament injury is one of the common sports injuries, which may result in joint instability and dysfunction [1,2]. In the United States, from 2002 to 2014, the overall rate of anterior cruciate ligament (ACL) reconstruction increased by 22 %, from 61.4 per 100,000 person-years (PYs) in 2002 to 74.6 per 100,000 PYs in 2014. The rates of ACL reconstruction in adolescents aged 13 to 17 years increased dramatically over the 13-year study period (isolated, +37 %; ACL + meniscal repair, +107 %; ACL + meniscectomy, +63 %) [3]. Patients whose symptoms cannot be relieved by the traditional treatment of ligament injury require surgical repair [4]. The gold-standard treatment for the surgical management of ligament injuries includes grafting of autologous tissues; which, is however complicated by the lack of the suitable numbers of transplantable autologous tissues and/or donor-site associated infection risks [5]. The use of the allogenic grafts is also limited by the immunogenicity risks [5,6]. Alternatively, tissue-engineered scaffolds have garnered considerable interest of the research community [7,8]. However, inherently less vascularity of ligament tissues impedes the regenerative response by limiting the availability of oxygen and nutrients [6–9]. Consequently, developing angiogenic scaffolds for the repair of ligament may hold great promise.

Growth factors play a vital role in tissue repair by effectively promoting cellular processes, such as cell viability, proliferation, and differentiation [10]. Being an integral component of vascular morphogenesis, vascular endothelial growth factor (VEGF) plays a crucial role in inducing neovascularization by promoting the growth, migration, and viability of endothelial cells (ECs) [11,12]. Accordingly, VEGF has been widely exploited for the treatment of ligament injuries [13–15]. However, being a large molecular weight protein, VEGF exhibits short half-life and poor retention at the injury site, which may abrogate its therapeutic benefits while posing additional side effects [16]. The localized and sustained presentation of growth factors at the injury site may avoid risks associated with their high concentration [17]. Additionally, being large molecular weight proteins, it is difficult to synthesize or incorporate growth factors into scaffolds [18]. On the other hand, short peptide sequences with the biological activity similar to the growth factors (GFs) may be beneficial to mimic the therapeutic benefits of GFs [19]. The *in vitro* or *in vivo* sequestration of GFs by using functional biomaterials is also an enticing avenue, which has been realized by installing GFs binding domains or peptides sequences into biomaterials [20]. Recently, Adini et al. demonstrated that the use of the specific prominin-1 derived VEGF binding peptide (BP) consisting of 12-amino acids (DRVQRQTTTVVA) can enhance the biological activity of exogenous and endogenous VEGF *in vitro* and *in vivo* to promote angiogenesis [19–21], while avoiding the potential risks of exogenously delivered or covalently-tethered GFs on scaffold materials [22,23]. Therefore, the method of grafting or adsorbing peptides on the surface of scaffold materials to sequester GFs may be of considerable significance to endow the scaffolds with the biological functions [24,25].

Herein, we hypothesized that the incorporation of BP into aligned electrospun nanofibrous scaffolds may orchestrate VEGF at the injury site, thus leading to a functional tissue repair. Electrospinning, being a versatile and a cost-effective technology for fabricating tissue-engineered scaffolds has received enormous interest of the scientific community [26]. The aligned nanofiber scaffolds prepared by electrospinning can guide the directional growth of tissues and organization of cells [27]. We have chosen biocompatible and biodegradable polycaprolactone/gelatin (PCL/Gel) hybrids as scaffold materials and adsorbed BP onto the surface of the fibers via van der Waals forces and hydrophobic interaction [28,29]. The VEGF binding ability of BP-adsorbed PCL/Gel nanofibers was discerned *in vitro* and potential of the scaffolds for the ligament regeneration was discerned *in vivo*. The functional scaffolds may orchestrate the endogenous VEGF at the injury site to promote neovessel formation and ligament regeneration, which may have broad applicability.

2. Experimental

2.1. Materials

PCL (M_w, 80 kDa) and gelatin from porcine skin (Type B, 48722-500G-F) were purchased from Sigma-Aldrich, Co., Ltd (Shanghai, China). 1,1,1,3,3,3-hexafluoro-2-propanol (HFIP) was acquired from Shanghai Darui Fine Chemical Co., Ltd. (Shanghai, China). Glutaraldehyde was obtained from Aladdin Bio-Chem Technology Co., Ltd. (Shanghai, China). Rhodamine-B conjugated BP (DRVQRQTTTVVA) was custom-synthesized by China Peptides Co., Ltd (Shanghai, China). The carboxyl groups (–COOH) of the rhodamine were conjugated to the N-terminus amino ($–NH_2$) groups of BP via an amide linkage. VEGF enzyme-linked immunosorbent assay (ELISA) kit was purchased from Beijing Solarbio Science & Technology Co., Ltd (Rat Vascular Endothelial Growth Factor ELISA Kit, SEKR0032, Beijing, China). The EA.hy926 cells were obtained from National Collection of Authenticated Cell Cultures (Shanghai, China). Human umbilical vein endothelial cells (HUVECs) were supplied by the Institute of Biochemistry and Cell Biology (The Chinese Academy of Sciences, Shanghai, China). All of the reagents and solvents were of commercial grade and used as received without any further purification.

2.2. Fabrication of PCL/Gel and BP@PCL/Gel Scaffolds

2.2.1. Fabrication of PCL/Gel Nanofibers

To prepare PCL/Gel scaffolds, PCL and Gel (4:6 w/w) were dissolved in HFIP to afford 10 % (w/v) solution. Aligned electrospun nanofibers were fabricated by electrospinning (Yongkang Leye Technology Development Co., Ltd. SS-3556H, Beijing, China). The electrospinning parameters were as follows: Syringe, 10 mL, needle size, 21G, flow-rate 1.5 mL/h; voltage, 10.0 kV, distance between the tip of the spinneret and the drum collector (diameter, 100 mm) was ~ 10 cm; collector speed, 2000 rotations per minute (rpm). The electrospinning was continued for up to 4 h at ambient temperature (~ 25°C) and relative humidity was in the range of 45–50 %. Electrospun scaffolds (thickness, 0.25–0.55 mm) were dried under vacuum, cross-linked with glutaraldehyde vapours for up to 30 min and stored for the subsequent use.

2.2.2. Fabrication of BP@PCL/Gel Scaffolds

To afford BP@PCL/Gel scaffolds, BP (1.0 mg) was dissolved in 10 mL of phosphate-buffered saline (PBS) to afford a peptide concentration of 0.1 mg/mL, which was homogenized by using a vortex mixer. While being protected from the light, PCL/Gel scaffolds were completely immersed in the BP solution for up to 2 h for the adsorption of the peptide. To ascertain the adsorption of BP on scaffolds by fluorescence method, different concentrations of BP (e.g., 0.005, 0.01, 0.02, 0.04, 0.08, and 0.1 mg/mL) were used. On the other hand, for VEGF binding assay *in vitro*, different concentrations of BP (0.0125, 0.025, 0.05 mg/mL, and 0.1 mg/mL) were used for adsorption.

2.3. Morphology of PCL/Gel and BP@PCL/Gel Scaffolds

The scaffolds (10 mm × 10 mm) were immersed in PBS or BP solution (0.1 mg/mL) and freeze-dried, and sputter-coated with gold for up to 45s. The morphology of scaffolds was discerned by scanning electron microscopy (SEM, Hitachi TM-1000, Japan) at an accelerating voltage of 5 kV. Image J software (National Institutes

of Health, v1.8.0, USA) was used to assess the average fiber diameter ($n = 100$) and angle distribution ($n = 100$) of nanofibers based on the SEM images. About, 100 nanofibers were randomly selected from the 5 area of a 1500X SEM picture to measure the diameter and angle distribution of nanofibers. Amongst, the angle distribution of nanofibers refers to the absolute value to the horizontal axis [5,30].

2.4. Characterization

2.4.1. TGA and DSC

The thermogravimetric analysis of both types of membranes (PCL/Gel and BP@PCL/Gel) was carried out by using a Thermogravimetric Analyzer (PerkinElmer Enterprise Management (Shanghai) Co., Ltd., TGA8000, Shanghai, China). The analysis was carried out at a heating rate of 15°C/min from room temperature for up to 800°C. The thermogravimetric parameters, including maximum degradation temperature (T_{max}) were analyzed by the TGA curves. For differential scanning calorimetry (PerkinElmer Enterprise Management (Shanghai) Co., Ltd., DSC8500, Shanghai, China), the heating rate was controlled at 10°C/min and samples were scanned from room temperature for up to 250°C. The thermodynamic properties of different scaffolds were analyzed by DSC curves.

2.4.2. Porosity

The total porosity (P) of scaffolds was determined by using a liquid displacement method [31]. Samples were prepared into rectangular shapes (20 mm × 20 mm × 0.25 mm) and weighed as "W_0". Afterwards, scaffolds were transferred into absolute ethanol for up to 6 h and then placed on the filter paper to remove the residual ethanol. The weight of the scaffolds was recorded as "W_1". The porosity of scaffolds was determined by the following Eq. (1):

$$P = \frac{(W_1 - W_0)}{(\rho \times V)} \quad (1)$$

where W_0 and W_1 represent weight of the scaffolds before and after soaking in the ethanol, respectively, ρ represents the density of the ethanol at room temperature, and V the volume of the wet scaffold ($n = 5$).

2.5. Adsorption property of BP In Vitro

The fluorescence intensity of BP@PCL/Gel scaffolds fabricated by using different concentrations of BP (e.g., 0.005, 0.01, 0.02, 0.04, 0.08, and 0.1 mg/mL) was detected by confocal laser scanning microscopy (CLSM, Carl Zeiss LSM700, Jena, Germany). The images were collected by using the same parameters at the scanning depth of 0.1–0.3 mm of scaffold thickness. The Zeiss ZEN software (ZEN 2.3, blue version) was used to calculate the fluorescence intensity of three random square sites (20 μm × 20 μm) of the collected pictures ($n = 3$).

2.6. Elucidation of the binding of BP@PCL/Gel Scaffolds with VEGF

About 2 nano grams (ng) of VEGF was dissolved in 10 mL of standard diluent (available with the VEGF ELISA kit) to afford VEGF solution with a concentration of 0.2 ng/mL. The BP@PCL/Gel scaffolds containing different concentrations of BP (0.0125, 0.025, 0.05, and 0.1 mg/mL) were immersed in VEGF solution at 37°C for up to 2 h. Afterwards, scaffolds were rinsed with PBS three times to obtain VEGF bound scaffolds. Subsequently, scaffolds ($n = 5$) were transferred to a 1.5 mL Eppendorf tube containing 0.3 mL of standard diluent as available with the VEGF ELISA kit and placed into a shaker for up to 2 h to facilitate the VEGF release at 37°C. The VEGF release was studied by using a Rat VEGF ELISA Kit following manufacturer's instructions. The optical density (OD) was measured by an ELISA plate reader (Thermo Fisher Technology (China) Co., Ltd., 1410101, Multiskan™ FC, Shanghai, China) at 450 nm.

2.7. Evaluation of the degradation of Scaffolds In Vitro

Degradation of the scaffolds was also measured by following a previous report with a slight modification [32]. Samples were cut into rectangular shapes and weighed under dry conditions (W_0). Subsequently, samples were placed in EP tubes containing 3 mL of PBS as a degradation medium and incubated at 37°C at 120 rpm. At pre-determined time points, the samples were rinsed with deionized water 3 times, freeze-dried, and weighed again (W_t). The remained mass percentage ($n = 4$) was determined by the following Eq. (2):

$$\text{Remained mass } (\%) = \frac{W_t}{W_0} \times 100\% \quad (2)$$

where W_0 and W_t represent the weight of the samples before and after degradation, respectively.

2.8. Mechanical properties

Mechanical properties of PCL/Gel and BP@PCL/Gel scaffolds (20 mm × 10 mm; thickness 0.28 ± 0.03 mm) were evaluated in wet state by using a universal tensile testing machine (Instron-5542, Canton, USA) with a 200 N load cell (Transcell Technology, Inc., BAB-20MT, USA) (Fig. S1). Specimens were immersed in the PBS for up to 10 min before analysis. An adhesive paper was used (5 mm on both ends) to fix samples into the grips. The gauge length of samples was recorded as the distance between the upper and lower grip. The specimen dimensions, such as thickness and effective testing length (L) were measured by using a vernier caliper before the test. All samples were tested at a fixed strain rate of 5 mm/min at room temperature until their breakage ($n = 5$).

The force-displacement curves were converted into stress-strain curves by using two different approaches [33,34]. In the first one, the apparent stress, calculated by dividing the force by the cross-sectional area (A) of the specimen measured before the test, was plotted against strain. While in the second approach, net mechanical properties of scaffolds were measured; the net stress was calculated by dividing the apparent stress by the volume fraction (v) of the specimens [35]. The volume fraction (v) of specimens was calculated by using the Eq. (3):

$$v = \frac{w}{(L \times A \times \rho)} \quad (3)$$

where *w, L*, and *A* represent the weight, length, and the cross-sectional area of the specimen. The ρ represented the density of the raw PCL/Gel material (4/6, w/w) ($\rho = 1.31$ g cm^{-3}), which was evaluated by using Archimedes' principle (supplementary information) [36].

The following mechanical parameters were calculated: modulus of elasticity (*E*), load force (FF), yield stress (σy), failure Stress (σf), unit work to yield (Ly), and unit work to failure (Lf) [34].

2.9. Cell culture

The EA.hy926 cells and HUVECs were cultured in Dulbecco's modified eagle medium (DMEM) supplemented with 100 U/mL penicillin, 0.1 mg/mL streptomycin, and 10 % fetal bovine serum (FBS) in an incubator at 37°C and 5 % CO_2.

2.10. Evaluation of the biocompatibility of Scaffolds In Vitro

The scaffolds of appropriate size were placed in a 24-well cell culture plate, washed with deionized water, and sterilized by immersing in 75 % (v/v) ethanol for up to 2 h. Subsequently, the scaffolds were washed with PBS two times each for up to 15 min to remove the residual ethanol. The EA.hy926 cell suspension (1.0×10^4 cells/well) was seeded onto the surface of the scaffolds and incubated at 37°C, 5% CO_2 for up to 1, 3, and 7 d. At each time point, the cell viability was assessed by cell counting kit-8 (CCK-8, C0038, Beyotime, China) by following the manufacturer's instructions. The optical density (OD) of samples was measured at 450 nm by an ELISA plate reader (Epoch™, BioTek, USA) at 450 nm ($n = 3$).

To assess the cell morphology and cell density, cell-seeded scaffolds were fixed by 2.5 % glutaraldehyde solution (Solarbio, China) and stained with fluorescein isothiocyanate-Phalloidin (FITC, CA1620, Solarbio, China) and 4',6-diamidino-2-phenylindole (DAPI, C0065, Solarbio, China) and observed by CLSM (Nikon C2, Japan) (supporting information). For morphological analysis, the scaffolds were dehydrated with graded ethanol series and sputter-coated with gold at 5 mA for up to 60 s and observed by SEM (Phenom ProX, Netherlands) (supporting information).

2.11. Scratch wound healing assay In Vitro

A scratch wound healing assay was performed to evaluate the effect of BP on cell migration *in vitro* [37]. HUVECs were seeded into 24-well plates and cultured for up to 12 h to afford a confluent monolayer. Afterwards, a scratch of approximately 160 μm was created on the confluent monolayer by using a pipette tip and the scratched cells were gently washed with PBS two times. Then, every group received 1.5 mL of low-serum conditioned medium and cells were cultured for up to 24 h and imaged by using an optical microscope (TS100, Nikon, Japan). The conditioned medium was collected by soaking PCL/Gel and BP@PCL/Gel scaffolds in the low-serum (1 % FBS) medium for up to 12 h. The conditioned medium from the BP@PCL/Gel-VEGF group was collected by first soaking the scaffolds in VEGF (200 pg/mL) for up to 2 h followed by incubating in the low-serum medium for up to 12 h. Images of the migrated cells were collected at 0 h and 24 h of culture by using a microscope (TS100, Nikon, Japan), and quantitatively analyzed by using Image J (NIH, v1.8.0, USA) to determine the area of the initial scratch (S_0) and healed scratch (S_1). The cell migration ratio was determined by the following Eq. (4):

$$\text{Migration ratio} = \left(1 - \frac{S_1}{S_0}\right) \times 100\% \quad (4)$$

2.12. Tubular formation of EA.hy926 cells treated with BP@PCL/Gel Scaffolds In Vitro

The Matrigel™ (356234, BD Matrigel, USA) was prepared at 4°C overnight. About 50 μL of the Matrigel was added to the bottom of a pre-cooled 96-well plate in each well and incubated at 37°C, 5% CO_2 for up to 30 min. To discern the effect of the BP on neovessel formation *in vitro*, PCL/Gel and BP@PCL/Gel scaffolds (0.45 mm × 15 mm × 15 mm) were soaked in VEGF solution (25 ng/mL) for up to 24 h [4]. The VEGF and standard diluent were used as available with the VEGF ELISA kit. Thereafter, the Scaffolds were rinsed twice with PBS for up to 3 min each. Afterwards, VEGF-immobilized PCL/Gel and BP@PCL/Gel scaffolds were soaked into 2 mL of PBS and incubated at 37°C, for up to 24 h to afford scaffolds' extract solution. For tubular formation assay, about 100 μL of EA.hy926 cells (1.5×10^4 cells/well) were cultured in a 96-well plate containing Matrigel and 100 μL of the scaffolds' extract solution and incubated for 12 h. The formation of the capillary-like structure was observed via a light microscope (DP72, Olympus, Japan). Then, network parameters of the capillary-like structures, such as the nodes, total branching length, and circles were analyzed and quantified by using Image J (File-open-Angiogenesis Analyze and Analyze HUVEC Phase Contrast) (NIH, v1.8.0, USA) ($n = 3$). The total branch length of PCL/Gel group was set as a reference and was compared with the other groups to afford the normalized total branching length.

2.13. Animal experiments

In this study, animal experiments were carried out with the approval of the Welfare and Ethics Committee of the Laboratory Animal Science Department of Fudan University. Sprague–Dawley rats ($n = 24$, male, weight, 190-210 g, age, 6 weeks) were randomly divided into three groups to receive PCL/Gel scaffold in one leg and BP@PCL/Gel scaffold in the other leg for 1, 2, and 4 weeks). Animals were anaesthetized with isoflurane (2 % for the induction and 1 % for the maintenance) and a single dose of 5 mg/100 g ketamine IM following our previous report [38]. Every rat received. Both patellar ligaments of the rats were exposed under anesthesia, and a 7×2 mm^2 full-thickness window defect was created in the central region of the patellar ligament without bony defect. Subsequently, PCL/Gel or BP@PCL/Gel scaffold (7 mm × 2 mm × 0.45 mm) was implanted into the defect. The fiber direction of the PCL/Gel and BP@PCL/Gel scaffolds was consistent with the longitudinal axis of the patellar ligament. After that, two stitches (6-0 silk suture) were sewn on the upper and lower ends of scaffolds to pass the suture through the patellar ligament and the scaffolds at the same time to avoid the detachment of the graft during implantation.

2.14. Immunohistochemistry and histopathological analysis

At 1, 2 and 4 weeks, the rats were sacrificed by an overdose intraperitoneal injection of 10 % chloral hydrate and the patellar ligament specimens regenerated with PCL/Gel or BP@PCL/Gel scaffolds were harvested and fixed in 4 % paraformaldehyde (PFA) immediately. Patellar ligaments without patella and femur were gradually dehydrated, embedded in paraffin, sectioned to 4 μm in thickness, and stained with CD31 (1:100, Abcam, UK), hematoxylin and eosin staining (H&E), and Picrosirius Red staining (PSR). The CD31 was used to identify endothelial cells and PSR was used stain collagen fibrils. For CD31 staining, the polarized light microscope (DM2500P, Leica, Germany) with 100X magnification was used to observe the stained sections. Each section was placed vertically at the same observation angle. The images were collected from regions centered on the scaffold and CD31 positive cells were qualitatively analyzed by Image J ($n = 3$, National Institutes of Health, v1.8.0, USA). To eliminate the influence of scaffold and interstitial space for PSR staining, the ratio of yellow collagen fibers to the green collagen fibers was also analyzed by Image J ($n = 3$, National Institutes of Health, v1.8.0, USA). The H&E staining sections were observed by the light microscope (DP72, Olympus, Japan).

2.15. Biomechanical test

After 1, 2, and 4 weeks of the implantation of scaffolds, the rats were sacrificed by an overdose intraperitoneal injection of 10 % chloral hydrate, and the bone-patellar ligament-bone complex was collected for biomechanical assessment. The patellar ligaments were trimmed to 4 mm width, and the cross-sectional areas of the patellar ligament and scaffolds was measured by a Vernier caliper. A universal mechanical instrument (Instron 5966, USA) at a fixed rate of 0.2 mm/min was used for the biomechanical test. The definition of failure was the rupture of the patellar ligament. The failure force (N) and tensile strength (MPa) were automatically calculated from the load-deformation curve ($n = 5$) by the the software

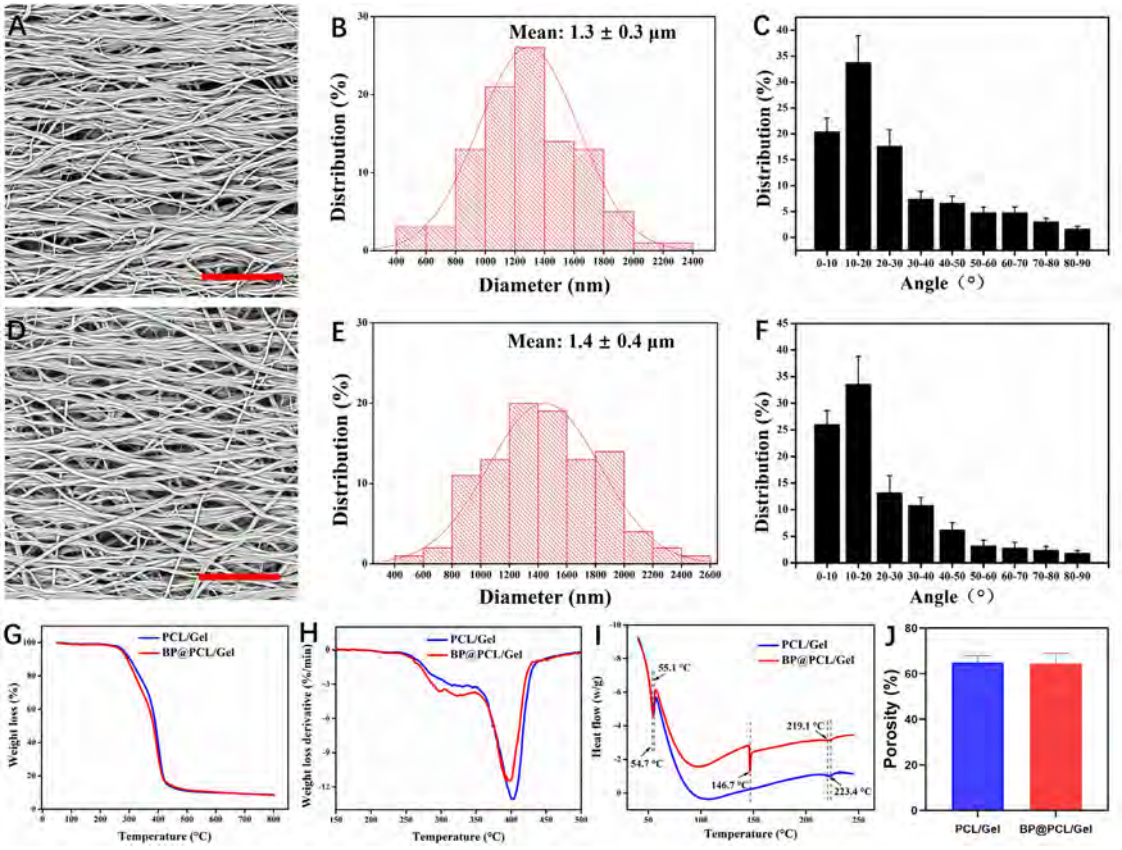

Fig. 1. Characterization of the aligned scaffolds. SEM images (A), diameter distribution (B), and fiber angle distribution (C) of PCL/Gel. SEM images (D), diameter distribution (E), and fiber angle distribution (F) of BP@PCL/Gel. TG curve (G), DTG (H), DSC (I), and porosity (J) of scaffolds. The scale bars of (A) and (B) are 50 μm.

(Bluehill Universal, Norwood, MA, US). The Young's modulus (E) was calculated from the linear region of the stress-strain curve. The biomechanical properties of native patellar ligament tissues were also measured, which served as a positive control. It is noteworthy to mention here that the biomechanical properties of injured patellar ligaments without the implantation of scaffolds (negative control) were reported previously and used as a reference [4].

2.16. Statistical analysis

All quantitative results were expressed as mean ± SD. Two-way ANOVA with Tukey's test and unpaired t-test was used to compare any significant difference among groups at different time points. GraphPad Prism Software v8.1 (San Diego, US) was used for the statistical analysis. Significant difference was considered at $^{*}p < 0.05$, $^{**}p < 0.01$, and $^{***}p < 0.01$.

3. Results

3.1. Characterization of PCL/Gel and BP@PCL/Gel Scaffolds

The morphology of PCL/Gel and BP@PCL/Gel scaffolds was discerned by SEM (Figs. 1A, 1D). Nanofibers were mainly aligned in the horizontal direction; few fibers were inclined (Fig. S2). Since for the immobilization of BP, scaffolds were immersed in the BP solution, we also assessed the morphology of PCL/Gel and BP@PCL/Gel scaffolds after incubation in PBS and BP solution, respectively. Both types of scaffolds displayed wavy fibers after immersion into the PBS or the BP solution, which is ascribed to the relaxation of polymer chains [39]. As can be seen from Fig. 1B and 1E, both PCL/Gel and BP@PCL/Gel scaffolds exhibited the narrow distribution of fiber size; the average diameter of the fibers was found to be 1.3 ± 0.3 μm and 1.4 ± 0.4 μm for PCL/Gel and BP@PCL/Gel nanofibers, respectively. A slight increase in the fiber diameter for BP@PCL/Gel scaffolds may be ascribed to the adsorption of BP on the fibers.

To ascertain the alignment of fibers in the scaffolds, the distribution of fiber angle was evaluated, which displayed that the fibers were mainly concentrated between 0–20° (0° refer to the fiber direction parallel to the horizontal axis). In the PCL/Gel group, 20 ± 3 % of the fiber angles were distributed between 0–10°, 34 ± 5 % between 10–20°, and 18 ± 3 % between 20–30°. On the other hand, in the BP@PCL/Gel group, 26 ± 3 % of the fiber angles were distributed between 0–10°, 34 ± 5 % between 10–20°, and 14 ± 3 % between 20–30° (Figs. 1C, 1F). These results demonstrated that the concentration of the fiber angle distribution of the two groups was high, and more than 85 % of the fiber angles were concentrated between 0–30°, which indicated that most of the fibers were aligned in the parallel direction similar to the natural ligament structures [5]. Altogether, there was no significant difference in the fiber angle distribution between PCL/Gel and BP@PCL/Gel scaffolds, which further indicated that the adsorption of BP did not affect the fibers' alignment and morphology.

TGA curves of PCL/Gel and BP@PCL/Gel scaffolds were displayed in Fig. 1G–H. The maximum degradation temperature (T_{max}) of PCL/Gel and BP@PCL/Gel scaffolds was found to be 404°C and 397°C, respectively (Fig. 1G–H). Moreover, BP@PCL/Gel scaffolds exhibited mass loss at slightly low temperature than that of PCL/Gel scaffolds (e.g., 5 % mass loss, PCL/Gel, 282°C and BP@PCL/Gel, 275°C), which may be ascribed to an earlier degradation of BP (Table S1, Supporting Information) [40]. As can be noticed from the

DSC curves (Fig. 1I), PCL/Gel scaffold exhibited two melting point peaks at 55°C and 223°C. On the other hand, BP@PCL/Gel scaffold exhibited three melting point peaks at 55°C, 147°C and 249°C, which is attributed to the existence of BP in the BP@PCL/Gel scaffold. Both types of scaffolds did not appreciably differ in terms of the porosity, which was found to be 65 ± 3 % and 65 ± 4 % for PCL/Gel and BP@PCL/Gel scaffolds, respectively (Fig. 1J).

Fig. S3 indicated the FTIR spectra of BP, PCL/Gel, and BP@PCL/Gel scaffolds. BP exhibited bands at 1626 cm^{-1} and 1530 cm^{-1}, which are ascribed to the amide I and amide II bonds, respectively [39]. PCL/Gel also displayed bands at 1639 cm^{-1} and 1537 cm^{-1}, which are ascribed to the amide I and amide II bonds, respectively. These bands were slightly shifted toward higher wavenumber (1644 and 1551 cm^{-1}) in BP@PCL/Gel scaffolds [30]. Overall, FTIR results confirmed the existence of the component in the scaffolds as well as the successful adsorption of BP on scaffolds (Fig. S3, supporting information).

Moreover, the atomic percentages of different elements, such as carbon, oxygen, and nitrogen as well as oxygen-to-carbon (O/C) ratio in BP, PCL/Gel, and BP@PCL/Gel scaffolds were analyzed by using XPS (Fig. S3). PCL/Gel and BP@PCL/Gel scaffolds did not appreciably differ in terms of the C, N, and O content and exhibited almost similar content of these elements.

The water contact angle of PCL/Gel and BP@PCL/Gel was measured (Fig. S4). The contact angle was found to be 20 ± 2 ° and 18 ± 1 ° for PCL/Gel and BP@PCL/Gel scaffolds, respectively, indicating that both types of scaffolds exhibited good hydrophilicity (Fig. S4, Supporting Information).

To ascertain the adsorption of BP on PCL/Gel scaffolds by using CLSM, rhodamine B was conjugated with the BP via an amide linkage between the carboxylic (–COOH) groups of rhodamine and the amino ($–NH_2$) groups of BP (Fig. 2). As can be observed from Fig. 2A, the fluorescence intensity of scaffolds increased with an increase in the concentration of the BP solution. The fluorescence intensity of the BP@PCL/Gel scaffolds was the highest at the BP concentration of 0.08 mg/mL as compared to the other groups (Fig. 2C). Moreover, the VEGF binding ability of BP containing scaffolds was discerned *in vitro* and shown in Fig. 2D. The amount of VEGF adsorbed on the scaffolds increased with an increase in the concentration of the BP solution (Fig. 2D). BP@PCL/Gel scaffolds showed significantly higher adsorption of VEGF than that of their counterparts devoid of BP (Table S2–S3, Supporting Information). The VEGF calibration curve is shown Fig. S5 (Supporting Information).

The degradation of scaffolds was also evaluated *in vitro*. As can be seen from Fig. 2B, PCL/Gel and BP@PCL/Gel scaffolds degraded faster during the first 10 days, which slowed down afterwards. The residual mass of scaffolds was found to be 72 ± 7 % and 74 ± 7 % for PCL/Gel and BP@PCL/Gel at day 30, respectively (Fig. 2E).

Next the mechanical properties of PCL/Gel and BP@PCL/Gel scaffolds were measured and shown in Fig. 3 and Table S4. The stress-strain curves of scaffolds displayed a non-linear toe region (Fig. 3A, up to 3–5% strain), analogous to the non-linear behavior of natural fascicles of tendons and ligaments [41]. After the toe region, both groups exhibited a similar linear elastic behavior analogous to the behavior of the natural tendons and ligaments [35]. After yield point, both types of scaffolds displayed a ductile behavior, reaching the high strain (for up to 130 %) before failure (Fig. 3B–C). Both types of scaffolds did not appreciably differ in terms of the different types of mechanical parameters, including yield stress (σy), failure stress (σf), yield strain, Young's modulus (E), work to yield (Ly), and work to failure (Lf), which indicates that the modification of electrospun nanofibers with the BP has a negligible effect on the mechanical properties of scaffolds (Fig. 3D–I and Table S4). We also assessed net mechanical properties of scaffolds by taking into consideration their volume fraction. As can be seen from Fig. 3 and Table S4, net mechanical properties of scaffolds were significantly higher than that of the apparent mechanical properties, which is in agreement with the previous reports [33,35].

3.2. *Biocompatibility assessment* In Vitro

The biocompatibility of PCL/Gel and BP@PCL/Gel scaffolds was assessed by using EA.hy926 cells and shown in Fig. 4. The CCK-8 assay revealed that the cell viability was not affected by the incorporation of BP into scaffolds; the OD value increased with an increase in the culture time in both types of scaffolds (Fig. 4C & Table S5, Supporting Information) [42,43]. PCL/Gel and BP@PCL/Gel scaffolds did not significantly differ in terms of cell viability from each other.

The cell morphology and cell density were further assessed by CLSM and SEM (Fig. 4A–B). The cell density on the surface of scaffolds increased with an increase in the culture period; cells spread and elongated along in the fiber direction as exhibited by SEM micrographs (Fig. 4A). However, PCL/Gel and BP@PCL/Gel scaffolds did not show significant difference in terms of the cell morphology. The CLSM further delineated that the EA.hy926 cells was stretched along the direction of fibers in both groups (Fig. 4A).

An *in vitro* scratch wound healing assay was performed to discern the effect of the BP on cell migration (Fig. 5). While exhibiting a similar initial wound depth, the conditioned medium obtained from BP@PCL/Gel and BP@PCL/Gel-VEGF scaffolds exhibited significantly higher migration of cells at 24 h (TCP, 27 ± 4 %, PCL/Gel, 36 ± 6 %, BP@PCL/Gel, 48 ± 4 %, BP@PCL/Gel-VEGF, 63 ± 9 %) (Figs. 5A, 5C). Similalry, after 48 h, the conditioned medium obtained from BP@PCL/Gel and BP@PCL/Gel-VEGF scaffolds displayed significantly better migration of cells than that of the PCL/Gel scaffolds (Fig. S6; TCP, 62 ± 3 %, PCL/Gel, 77 ± 4 %).

The effect of BP@PCL/Gel scaffolds on angiogenesis was also evaluated by an *in vitro* HUVECs tube formation assay and the obtained results are shown in Fig. 5B. The EA.hy926 cells could form a capillary-like network structure 12 h following incubation in the Matrigel (Fig. 5B). The network parameters, such as nodes and total branch length were quantified by using image J. The red circles and the blue meshes represented the nodes and the circles, respectively, while the yellow lines and green lines together represented the total branching length in Fig. 5B. The normalized total branch length and the numbers of loops were significantly higher in BP@PCL/Gel scaffolds than that of the PCL/Gel scaffolds (Fig. 5D–F).

3.3. *Evaluation of angiogenesis* In Vivo

To evaluate the angiogenic ability and identify endothelial cells in PCL/Gel and BP@PCL/Gel scaffolds post-implantation, the CD31 staining was performed and the obtained results are shown in Fig. 6. As can be noticed from Fig. 6A, the CD31 positive staining of cells (ROI displayed in Fig. S7) gradually decreased from 1 week to 4 weeks after implantation; BP@PCL/Gel scaffolds showed neo-vessel formation exhibiting a distinct vascular morphology at 1 week. Besides, BP@PCL/Gel scaffolds displayed neovascularization 4 weeks after implantation.

3.4. *Histopathological analysis of regenerated patellar ligament*

H&E staining was performed 1, 2, and 4 weeks post-implantation to analyze the regeneration of the injured patellar ligament. As shown in Fig. 6B, the scaffolds were observed in PCL/Gel and BP@PCL/Gel groups for 4 weeks. The internal fibrous morphology of the scaffolds remained unaffected; scaffolds integrated well with the host tissue. No necrotic tissues were found. At 1 and 2

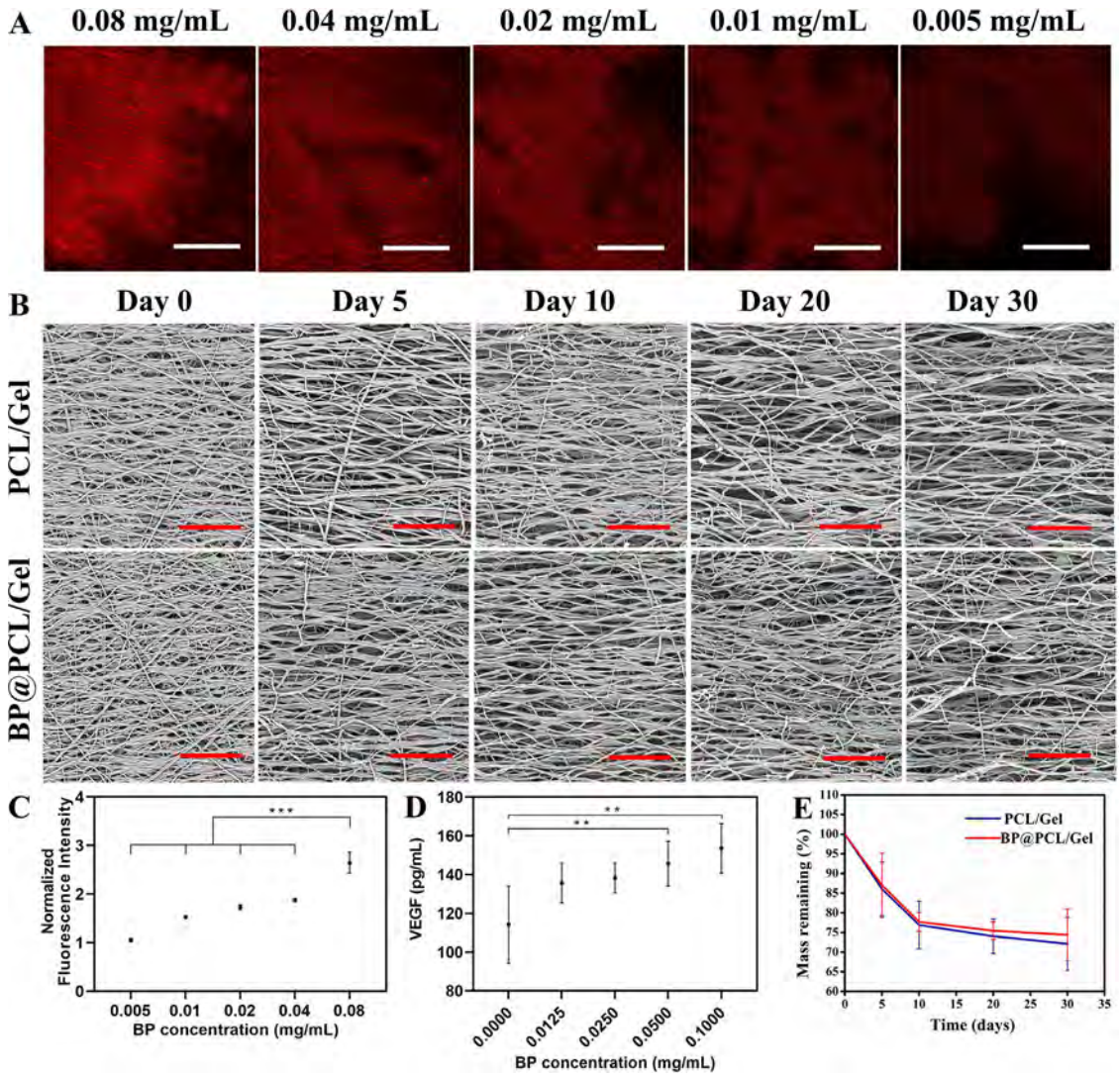

Fig. 2. Representative fluorescence images (A) of BP@PCL/Gel scaffolds by soaking in different concentrations of BP solution (0.08 mg/mL, 0.04 mg/mL, 0.02 mg/mL, 0.01 mg/mL and 0.005 mg/mL). Representative SEM images after the degradation of scaffolds for up to day 30 (B). Representative fluorescence intensity of PCL/Gel soaked into the BP solution of different concentration (C). Representative curve for the adsorption of VEGF by BP@PCL/Gel scaffolds *in vitro* (D). Mass remaining after degradation of PCL/Col and BP@PCL/Gel after degradation (E). $^{**}p < 0.01$, $^{***}p < 0.001$. The scale bars of (A) and (B) are 200 μm and 80 μm, respectively.

weeks after the implantation, infiltration of inflammatory cells was observed in both groups.

The PSR staining was performed to evaluate the regeneration of collagen fibers in regenerated patellar ligament tissues. As shown in Fig. 6C, thick collagen fibers showed strong birefringence, which were yellow and referred to as collagen type I, and thin collagen fibers showed weak birefringence, which were green and referred to as collagen type III under the polarizing microscope [44]. To eliminate the interference of scaffold and gap on the proportion of collagen fiber area, the type I/III collagen fiber area ratio was analyzed (Fig. 6E). It was found that the ratio of type I/III collagen fiber area in the BP@PCL/Gel scaffolds was significantly higher than that of the PCL/Gel group (ROI displayed in Fig. S7, Supporting Information) at 4 weeks post-implantation, which further indicated the maturity of the regenerated collagen induced by BP@PCL/Gel scaffolds.

3.5. *Biomechanical properties* In Vivo

To evaluate the functional recovery of the patellar ligament after the implantation of scaffolds, biomechanical tests were performed on the postoperative specimens of scaffolds. Native patellar tendon served as the positive control group, which displayed the failure force and tensile stress values of 64 ± 3 N and 6 ± 2 MPa, respectively. Besides, the biomechanical properties of injured patellar ligament without the implantation of scaffold (negative control) were used as a reference as reported previously [4]. The obtained results are shown in Fig. 7 and Table S6. The tensile stress-strain curves exhibited an initial stiffening and then softening, which can be ascribed to the use of full-window defect model *in vivo* (Fig. 7A) [5,45]. The cross-sectional area of patellar ligament specimens was measured before operation (Fig. 7B). The CSA of the native patellar tendon was found to be 2.75 ± 0.04 mm^2. The CSA of the both types of scaffolds decreased at week 4; the CSA of the BP@PCL/Gel scaffolds was significantly lower than that of the samples retrieved 1 week and 2 weeks after implantation. The failure force of the patellar ligament gradually increased from 1 to 4 weeks after the implantation of scaffolds (Fig. 7C; PCL/Gel: 1w, 17 ± 7 N, 2w, 41 ± 8 N, 4w, 52 ± 12 N; BP@PCL/Gel: 1w, 30 ± 6 N, 2w, 49 ± 7 N, 4w, 63 ± 16 N). On the other hand, the failure force of the negative control was found to be 19 ± 5 N, 30 ± 4 N, and 44 ± 8 N at 1, 2, and 4 weeks after surgery (Table S6, Supporting Information)

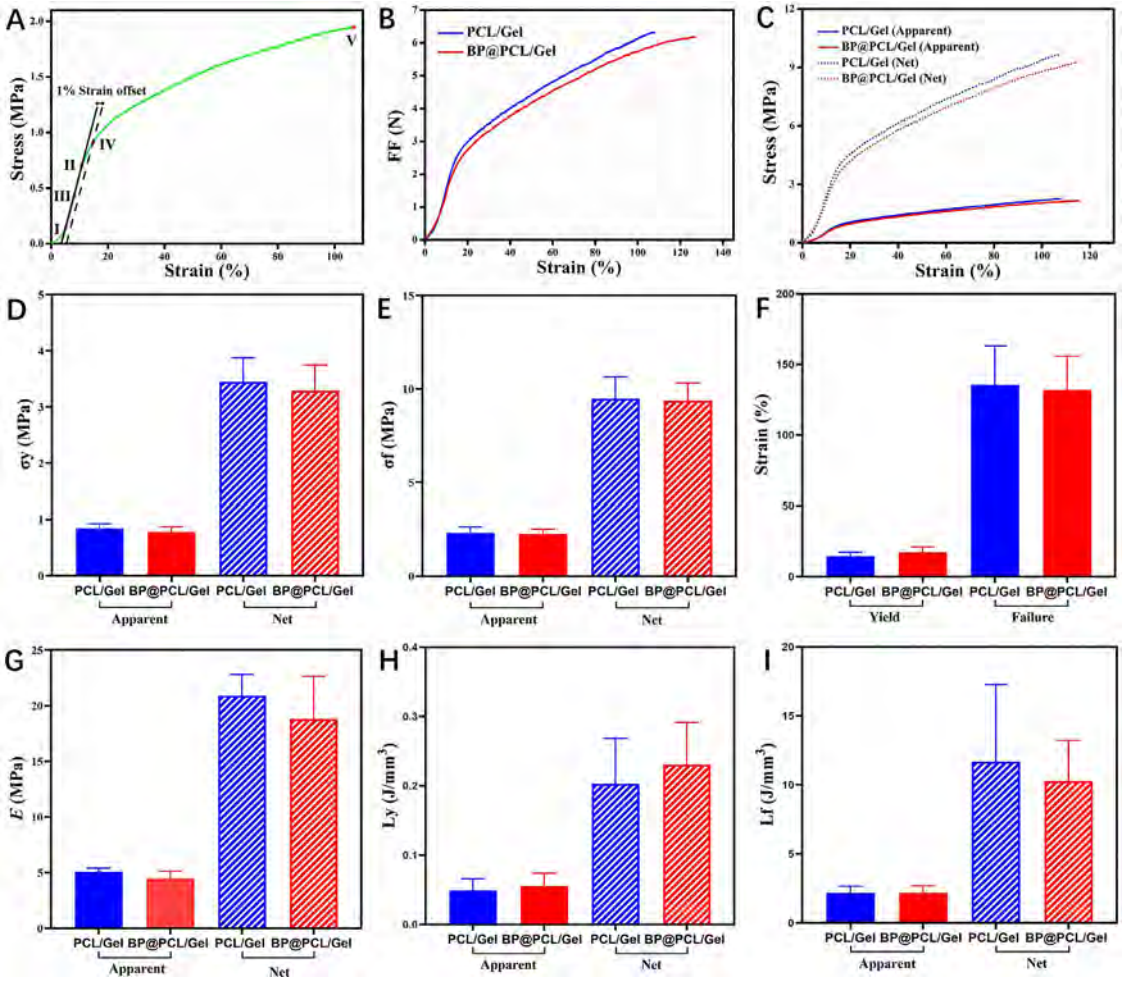

Fig. 3. Mechanical properties of PCL/Gel and BP@PCL/Gel scaffolds. (A) Representative diagram illustrating the post processing of the stress-strain curves for scaffolds. The failure stress (σf) (V) was identified as the highest stress in the entire stress-strain curve. The starting point of the linear region (I) was identified as the 10 % of the failure stress (f) for scaffolds. The initial toe region (from 0 N to I) was disregarded. An initial guess of the yield strain was visually identified (II). A first linear regression (solid line) was applied to the first 50 % of the linear region, between points (I) and (III) (III was half-way between I and II). A second line parallel to the first regression line was drawn with an offset of 1% strain (dashed line). The limit of proportionality was defined as the 1% strain offset criterion as the intersection (IV) between the latter line and the stress-strain curve. The modulus of elasticity (E) was calculated as the slope of a new regression line between (I) and (IV). The unit work to yield (Ly) and to failure (Lf) were calculated as the integrals under the curves (with the method of trapezoids). Two plots were obtained for each specimen: one reporting the apparent stress, the other one with the net stress. (B) Representative load vs. strain curves. (C) Representative apparent (solid lines) and net (dashed lines) stress–strain curves. Comparison between the mechanical properties of PCL/Gel and BP@PCL/Gel scaffolds: (D) Yield stress (σy), (E) Failure stress (σf), (F) Yield and Failure strain, (G) modulus of elasticity (E), (I) Unit work to yield (Ly), and (H) Unit work to failure (Lf).

[4]. As can be seen from these results, the implantation of scaffolds displayed better failure force than that of the negative control group which lacked implants. BP@PCL/Gel scaffolds displayed significantly higher failure force than that of the PCL/Gel scaffolds at 1 week after implantation (Fig. 7C). Similarly, the tensile strength of patellar ligament specimens in the BP@PCL/Gel group was significantly higher than that of the PCL/Gel group and the negative control group (Fig. 7D & Table S6; PCL/Gel: 1w, 1.6 ± 0.6 MPa, 2w, 3.7 ± 0.7 MPa, 4w, 5.6 ± 2.0 MPa; BP@PCL/Gel: 1w, 2.6 ± 0.5 MPa, 2w, 4.3 ± 0.6 MPa, 4w, 7.2 ± 2.2 MPa; negative control groups: 1w, 0.9 ± 0.6 MPa, 2w, 1.5 ± 0.8 MPa, and 4w, 3.4 ± 1.3 MPa) at 1-week post-implantation.

4. Discussion

VEGF, which plays an important role in angiogenesis, was identified, isolated, and cloned 32 years ago [46]. It has been confirmed that VEGF plays an important role in tissue repair by promoting the survival, migration, and proliferation of endothelial cells (ECs), and formation of neo-vessels *in vitro* and *in vivo* [47]. However, to achieve the reasonable concentration of VEGF that can induce vascularization, its high concentration may be required, which may induce potential toxicity risks, including edema and hemangioma formation [48,49]. The sustained and localized delivery of VEGF is therefore required to avoid toxicity risks associated with its high concentration. During tissue repair, VEGF is expressed at the injury site, which induces ECs proliferation and tubular formation [15]. However, due to the short half-life of VEGF, it can be easily cleared out from the injured tissues as well as it can be degraded by the matrix metalloproteinases, which require strategies for its stabilization and sustained signaling at the injury site for tissue repair. Therefore, pharmacological manipulation of VEGF to accelerate recovery may be a promising therapeutic approach that can accelerate tissue regeneration while avoiding the potential limitations associated with the exogenous delivery of VEGF or its excessive dosage.

Previously, different types of approaches have been put forwarded to afford VEGF sequestration at the injury site, including the design of heparin-tethered polymers as well as the incorporation of ECM domains capable of binding VEGF [10,14]. Adini et al.

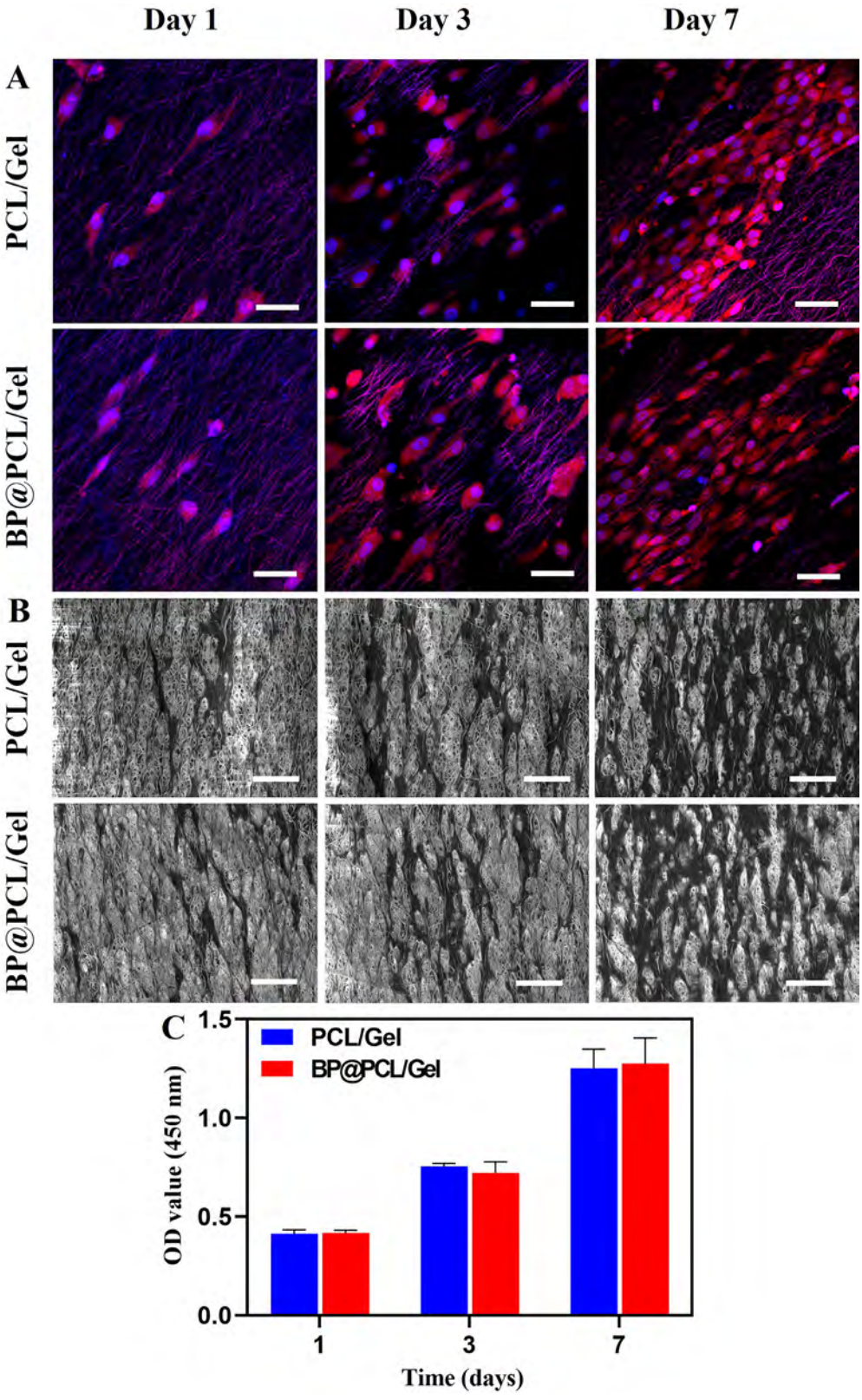

Fig. 4. Proliferation and morphology of EA.hy926 on PCL/Gel and BP@PCL/Gel scaffolds *in vitro*. Representative CLSM images (A) and SEM images (B) of EA.hy926 cultured on the scaffolds at 1, 3, and 7 days. Optical density (OD) values of EA.hy926 in scaffolds at 450 nm after being cultured for up to 1, 3, and 7 days (C). The scale bars of (A) and (B) are 20 μm and 50 μm, respectively.

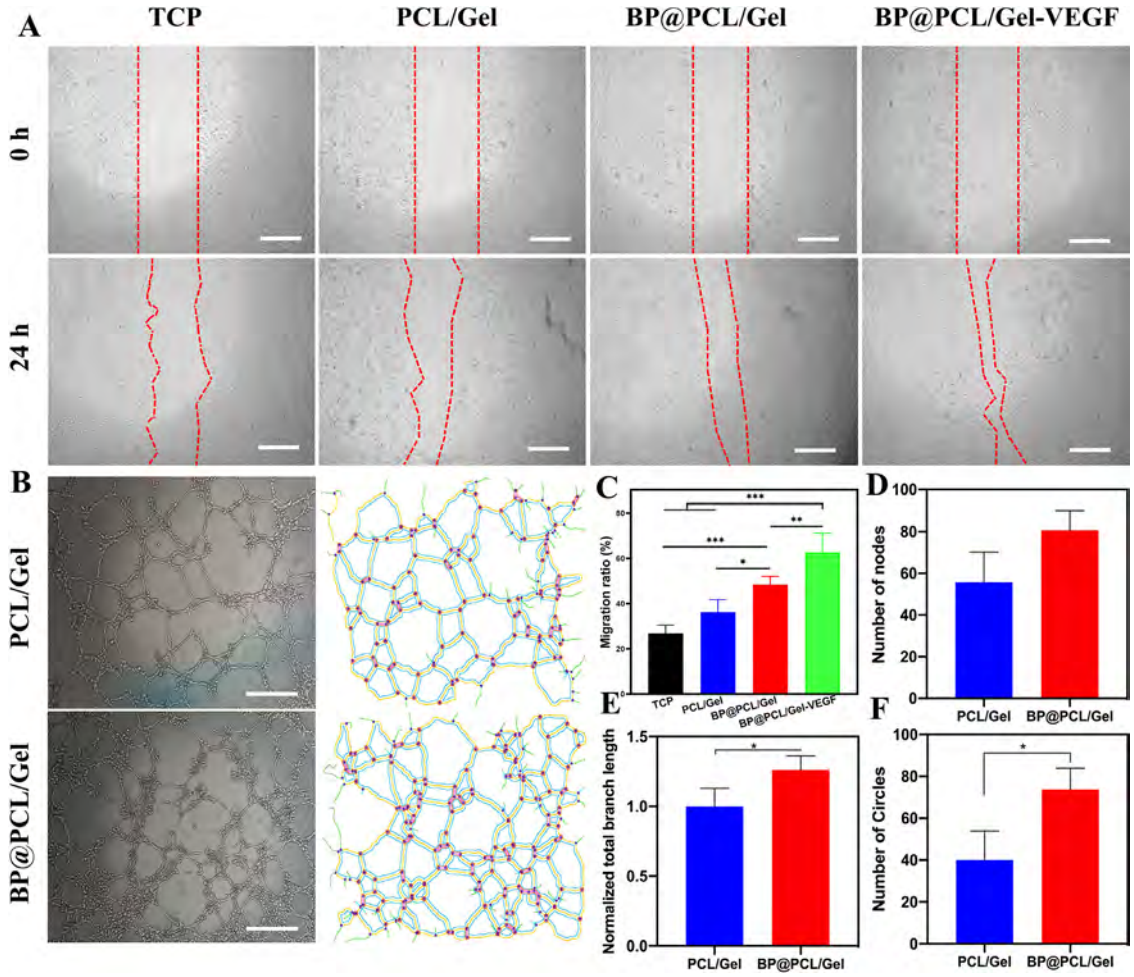

Fig. 5. Representative images of HUVECs migration at 0 h and 24 h in a scratch wound healing assay *in vitro* (A), and the tube formation of EA.hy926 cells *in vitro* (B) ($n = 3$). The quantitative analysis of the HUVECs migration ratios (C). The quantitative analysis of number of nodes (D), normalized total branching length (E), and number of circles of the tube formation of EA.hy926 cells (F). $^{*}p < 0.05$, $^{**}p < 0.01$, $^{***}p < 0.001$. The scale bars in (A) and (B) are 100 μm and 50 μm, respectively.

designed an amino acids sequence (DRVQRQTTTVVA) derived from the extracellular VEGF binding domain of glycoprotein prominin-1 and demonstrated its angiogenic effect *in vivo* [16,18]. It was further demonstrated that the BP can enhance the biological activity of VEGF by binding with the VEGF receptor-2 (VEGFR-2) and the neuropilin-1 (NRP-1) and promote angiogenesis [20]. We set out to leverage this approach to orchestrate VEGF at the injury site and immobilized BP on PCL/Gel based scaffolds, which may have advantages over the soluble form of the VEGF or systematically delivered BP. To afford CLSM observation and establish that the BP was successfully adsorbed on the scaffolds, Rhodamine B was conjugated with BP, which displayed an increase in the fluorescence intensity with an increase in the concentration of BP (Fig. 2A). Indeed our *in vitro* results established that the BP@PCL/Gel scaffolds accumulated more content of VEGF than that of their counterparts lacking BP (Fig. 2C); the VEGF content increased with an increase in the concentration of BP *in vitro* (Fig. 2D). The control scaffolds lacking BP also exhibited VEGF binding, which may be ascribed to the internal adhesion of the scaffolds [50]. These results together illustrate that BP can promote the accumulation of exogenous VEGF, which may also have implications for neovascularization *in vivo* given to the elevated expression of VEGF at the injury site following a tissue insult [50]. Our *in vitro* results establish that the scaffolds containing the BP did not induce an obvious cell cytotoxicity and that the BP@PCL/Gel induced tubule formation of ECs *in vitro* (Figs. 4 & 5B, D-F). Besides, BP@PCL/Gel scaffolds promoted wound healing *in vitro* (Fig. 5A & C).

Since adequate numbers of blood vessels are necessary for sufficient transport of oxygen and nutrients during tissue regeneration *in vivo*, promoting vascularization exhibits great promise for tissue engineering applications. While a myriad of strategies has been put forwarded for inducing vascularization in tissue-engineered scaffolds, such as ECs co-culture and the incorporation of growth factors into scaffold materials, these approaches are largely constricted owning to the limitations associated with the extensive manipulations of cells *in vitro* or their poor survival and engraftment at the targeted site after transplantation *in vivo* [51]. Besides, the difficulty in synthesizing large molecular weight proteins or incorporating them into scaffold materials further impedes this approach. Since BP exhibits potential to sequester or bind exogenous or endogenous VEGF within the tissue-engineered construct, the VEGF accumulation into the scaffold or at the injury site may lead to the higher numbers of neo-vessels formation [49,50].

Since ligaments lack adequate vascularization, which constrict the regeneration after an injury, promoting vascularization may have great potential for ligament regeneration [52]. Consequently, the effect of BP-mediated VEGF sequestration was further discerned for the HUVECs tubular formation and wound healing *in vitro*. The conditioned medium obtained from the BP@PCL/Gel scaffolds and BP@PCL/Gel-VEGF scaffolds facilitated HUVECs tubular

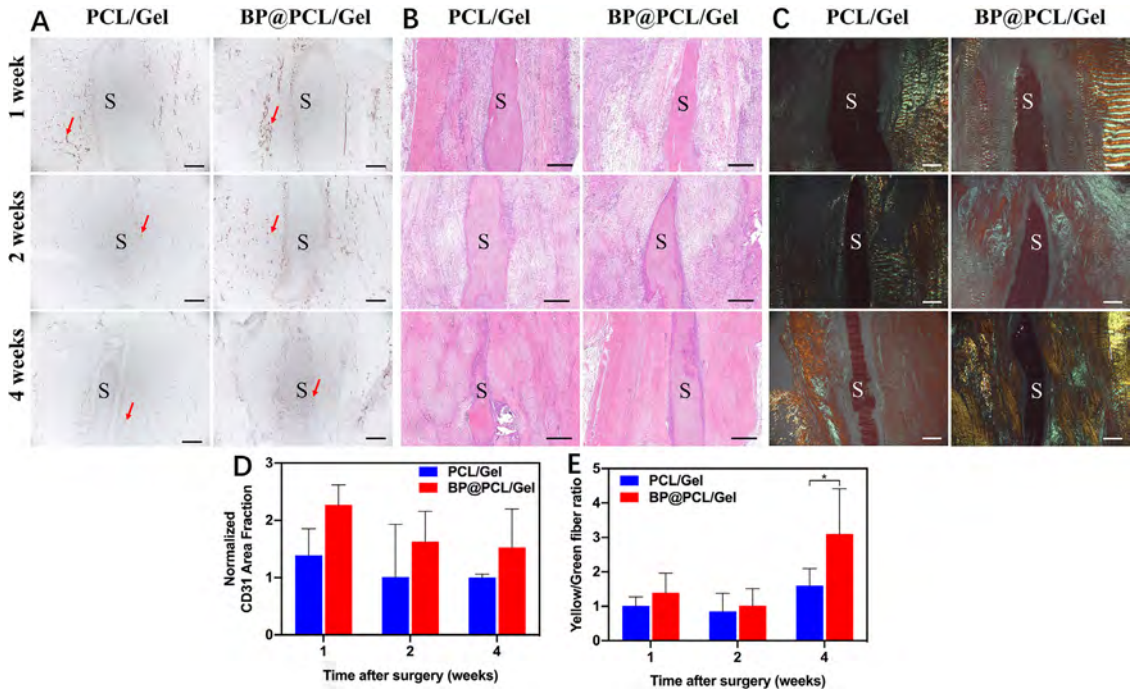

Fig. 6. Histopathological analysis of the regenerated patellar ligament 1, 2, and 4 weeks after the implantation of scaffolds. Representative images of CD31 staining (A), H&E staining (B), and PSR staining (C). Quantitative analysis of CD31-positive stained area (D). Quantitative analysis of the PSR staining for the ratio of yellow fibers to the green fibers ($n = 3$) (E). (S = Scaffold). The red arrows points toward new blood vessels. $^{*}p < 0.05$. Scale bar, 300 μm.

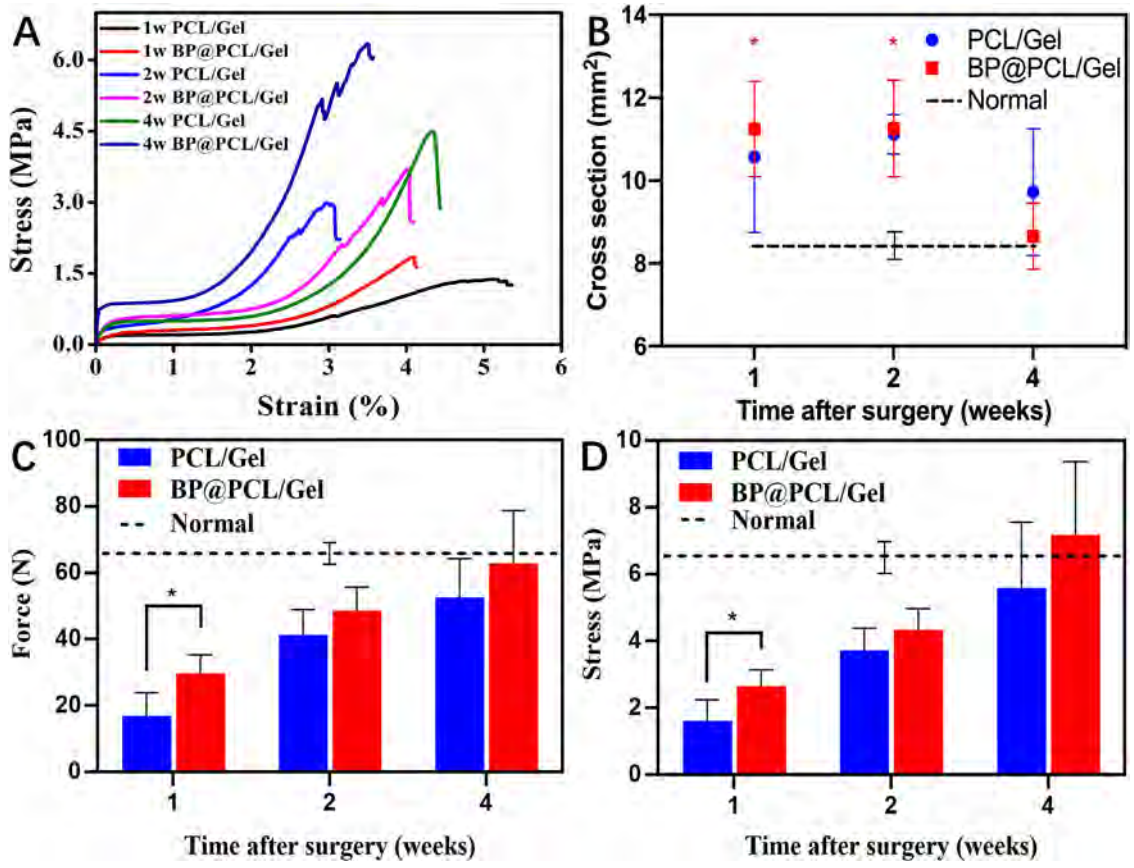

Fig. 7. Representative tensile stress-strain curves (A), the cross-sectional area (B), failure force (C), and tensile stress (D) of the regenerated patellar ligament in the PCL/Gel and BP@PCL/Gel groups 1, 2, and 4 weeks after implantation ($n = 5$). $^{*}p < 0.05$. Normal value represents the biomechanical properties of native patellar tendon without an injury.

formation as well as promoted wound healing *in vitro*, which were significantly higher than that of the PCL/Gel scaffolds. These results are attributed to the beneficial effect of BP on the VEGF binding and stabilization as well as its potential to promote the interaction of VEGF with its receptors, which may also have implications for improving neo-vessel regeneration *in vivo*. Adini et al. previously reported that BP-mediated amelioration of neo-vascularization was absent in a corneal pocket in the absence of the exogenous VEGF as compared to the injured corneal tissues, establishing that BP acts in a VEGF-dependent manner [19,20,23]. It has been found that the VEGF expression transiently increases at the site of the tissue injury and ischemia, such as myocardial infarction (MI), limb-ischemia in peripheral artery disease, and ischemic ulcers. However, given to the short half-life as well as rapid degradation by MMPs, the VEGF level returns to its baseline within a few hours [53–55]. Indeed, it was delineated that the BP improved outcome in different animal models, such as choroidal neovascularization model, hind-limb ischemia model, and MI model as well as enhanced the VEGF binding to its receptors, including VEGFR1 and neuropilin-1 [20,21]. Consequently, harnessing BP to interact with the VEGF, stabilize it, and increase its binding to its receptors may hold great promise to sustain VEGF signaling at the injury site while avoiding the toxicity risks associated with the VEGF protein or gene therapy [19,47,48].

The results of PSR staining provided a therapeutic basis for the promotion of the repair of damaged ligaments through angiogenesis. In this study, the average area ratio of type I/III collagen fibers in the BP group was significantly higher in BP@PCL/Gel scaffolds than that of the PCL/Gel group 4 weeks after implantation (Fig. 6E), indicating that the maturity of the collagen fibers in the BP@PCL/Gel scaffolds group was higher during ligament repair [56]. Among them, the ratio decreased at 2 weeks after surgery, probably because the tissues underwent a large number of new collagen synthesis stages [57]. Setiawati et al. also showed that exogenous injection of VEGF during ACL reconstruction could promote angiogenesis and contribute fibrous integration between tendon and bone during the early postoperative stage [50]. In addition, the effect of angiogenesis on the repair of damaged ligaments was also reflected in the biomechanical results.

Since the mechanical properties play a significant role for the performance of scaffolds for ACL reconstruction, a multitude of materials, including multiscale hierarchical scaffolds have been fabricated. We designed aligned PCL/Gel based scaffolds to better mimic the native patellar ligament tissues. The aligned PCL/Gel scaffolds exhibited stress-strain curves similar to the native tendon exhibiting a non-linear toe-region in agreement with the previous studies [33]. Moreover, these PCL/Gel and BP@PCL/Gel scaffolds exhibited mechanical properties comparable to the previous mats [5]. For instance, Sheng et al. reported failure load and *E* values of 5.4 $\pm$ 0.4 N and 65 $\pm$ 7 MPa in aligned PCL/Gel scaffolds (5:5 w/w) [4]. On the other hand, we observed failure load (6.3 $\pm$ 0.8 N and 6.3 $\pm$ 0.3 N) and *E* (170 $\pm$ 22 MPa and 147 $\pm$ 20 MPa) for PCL/Gel and BP@PCL/Gel scaffolds, respectively [4]. While the native tendon and ligament tissues display hierarchical architecture consisting of multiscale bundles wrapped by the sheath, further research is warranted to better mimic the morphology and architecture of the native tissues. As shown in Figs. 7B–C and Table S6, the failure force and tensile stress in PCL/Gel and BP@PCL/Gel groups increased with an increase in the implantation time; the latter exhibited significantly higher failure force and tensile strength than that of the PCL/Gel scaffolds 1 week post-surgery. By week 4, the implanted scaffolds exhibited tensile stress comparable to the native patellar ligament tissues. However, we noticed that the mechanical properties of our scaffolds were lower especially at the initial stage than that of the normal patellar ligament tissues. We observed an initial stiffening and then a softening in the stress-strain curves of implanted scaffolds, which could be ascribed to the use of the full-window defect model *in vivo* (Fig. 7A) [1,4,5]. We speculate that the tissue repair process is slow in this animal model and that during the mechanical evaluation, the initial stiffness is due to the scaffold implanted into the lesions. In the later stages, once the regenerated ligament tissues begin providing mechanical strength, this initial stiffness diminishes and regenerated tissues exhibit typical stress-strain curves. It is pertinent to mention here that scaffolds, especially, BP@PCL/Gel exhibited higher cross-section, failure stress, and tensile strength than that of the lesion without the implantation of scaffolds [4]. For instance, the failure force values of BP@PCL/Gel scaffolds were 30 $\pm$ 6 N, 49 $\pm$ 7 N, and 63 $\pm$ 16 N 1, 2, and 4 weeks after implantation, which were profoundly higher than that of the lesions only lacking the scaffolds (e.g., 19 $\pm$ 5 N, 30 $\pm$ 4 N, and 44 $\pm$ 8 N at 1, 2, and 4 weeks after surgery (Table S6)) [4]. Moreover, as compared with the findings of Sheng et al., who reported failure load of 344 $\pm$ 65 N in aligned PCL/Gel scaffolds 8 weeks after implantation in patellar ligament tissues, we observed less failure load (52 $\pm$ 12 N and 63 $\pm$ 16 N) in PCL/Gel and BP@PCL/Gel scaffolds, respectively, which can be attributed to a shorter implantation period [4].

Our study has also certain limitations. First, we did not evaluate the biomechanical properties of patellar ligament tissues post-injury at different time points. The evaluation of the biomechanical properties of injured patellar ligament tissues may be helpful for assessing the therapeutic benefits of the scaffolds. Nonetheless, we have previously measured the biomechanical properties of injured patellar tendon without implantation of scaffold, which delineated that the scaffolds provided a conducive environment for ligament tissues [30]. Secondly, we assessed only a narrow range of the concentration of BP; the optimization of the concentration of BP for VEGF orchestration is warranted for therapeutic angiogenesis. Thirdly, the normal patellar ligament tissues exhibit an ECM like architecture with the nano-sized fiber diameter. While we fabricated aligned electrospun PCL/Gel scaffolds reflecting the morphology of tendinous tissues, they did not accurately mimic the ECM of patellar ligament tissues and therefore warrant further design [5,27]. The collagen fiber bundles are a highly ordered hierarchical structure, ranging from collagen fibril to collagen fiber, with a span ranging from 50 nm to 100 μm [1,52,58]. Therefore, the nanofibers of the PCL/Gel and BP@PCL/Gel groups are still biomimetic. While we did not accurately replicate the native structure of collagen fibrils, we fabricated aligned scaffolds to mimic the orientation structure of collagen fibers in ligaments. Besides, we introduced BP into the scaffolds by simply immersing the latter into the BP solution, which however, may have limited stability and can be easily eluted from the scaffolds. The covalent tethering of VEGF-binding peptide may exhibit localized and sustained presentation, which may be beneficial for tissue repair applications. Taken together, our approach of immobilizing BP peptide on scaffolds for enhancing VEGF binding *in vivo* may have broad implications for tissue engineering applications.

5. Conclusions

In this study, the PCL/Gel based aligned nanofiber scaffolds were fabricated by electrospinning, which were next modified with the BP to enhance VEGF binding. The BP@PCL/Gel scaffolds exhibited biocompatibility, biodegradability, and VEGF-binding ability. The scaffolds containing BP facilitated HUVECs tubular formation and wound healing *in vitro*. The implantation of the BP containing scaffolds into an injured patellar ligament model in rats *in vivo* led to the regeneration of ligament tissues along with the formation of the mature collagen fibers than that of the scaffold only group. Given to the ubiquitous ability of VEGF to induce neovascularization, this strategy of sequestering exogenous or endogenous

VEGF by exploiting BP may have broad implications for tissue-engineered scaffold materials.

Declaration of Competing Interest

The authors declare that they have no known competing financial interests or personal relationships that could have appeared to influence the work reported in this paper.

Acknowledgments

This work was supported by the National Key R&D Program of China (2016YFC1100300), National Natural Science Foundation of China (Nos. 32050410286, 81772339, 81972129, 31771023, 81911530136, 81811530750, 82072521, 8217091186 and 82111530200), The Fundamental Research Funds for the Central Universities (2232019A3-07), The Key Clinical Medicine Center of Shanghai (2017ZZ01006), Sanming Project of Medicine in Shenzhen (SZSM201612078) and The Introduction Project of Clinical Medicine Expert Team for Suzhou (SZYJTD201714), Development Project of Shanghai Peak Disciplines-Integrative Medicine (20180101), Shanghai Talent Development Funding Scheme (2020080), Shanghai Committee of Science and Technology (19441901600, 19441902600, 20DZ2254900, 20S31900900 and 19441902000), Shanghai Sailing Program (21YF1404100), Sino German Science Foundation Research Exchange Center (M- 0263), National Advanced Functional Fiber Innovation Center (2021-fx020301), International Cooperation of 2021-2022 China, and Poland Science and Technology Personnel Exchange Program (No. 17). The authors gratefully acknowledge the due support from the team members of Prof. Xiumei Mo and Prof. Shiyi Chen.

Supplementary materials

Supplementary material associated with this article can be found, in the online version, at doi:10.1016/j.actbio.2021.11.040.

References

[1] J. Cai, X. Xie, D. Li, L. Wang, J. Jiang, X. Mo, J. Zhao, A novel knitted scaffold made of microfiber/nanofiber core-sheath yarns for tendon tissue engineering, Biomater. Sci. 8 (2020) 4413–4425, doi:10.1039/d0bm00816h.
[2] H. Li, C. Chen, S. Chen, Posttraumatic knee osteoarthritis following anterior cruciate ligament injury: Potential biochemical mediators of degenerative alteration and specific biochemical markers, Biomed. Rep. 3 (2015) 147–151, doi:10.3892/br.2014.404.
[3] M.M. Herzog, S.W. Marshall, J.L. Lund, V. Pate, C.D. Mack, J.T. Spang, Trends in incidence of ACL reconstruction and concomitant procedures among commercially insured individuals in the United States, 2002-2014, Sports Health 10 (2018) 523–531, doi:10.1177/1941738118803616.
[4] J. Chen, D. Sheng, T. Ying, H. Zhao, J. Zhang, Y. Li, H. Xu, S. Chen, MOFs-based nitric oxide therapy for tendon regeneration, Nano-Micro Lett. 13 (2021) 23, doi:10.1007/s40820-020-00542-x.
[5] D. Sheng, J. Li, C. Ai, S. Feng, T. Ying, X. Liu, J. Cai, X. Ding, W. Jin, H. Xu, J. Chen, S. Chen, Electrospun PCL/Gel-aligned scaffolds enhance the biomechanical strength in tendon repair, J. Mater. Chem. B 7 (2019) 4801–4810, doi:10.1039/c9tb00837c.
[6] A. Sensini, G. Massafra, C. Gotti, A. Zucchelli, L. Cristofolini, Tissue engineering for the insertions of tendons and ligaments: an overview of electrospun biomaterials and structures, Front. Bioeng. Biotechnol. 9 (2021) 645544, doi:10.3389/fbioe.2021.645544.
[7] A. Sensini, L. Cristofolini, Biofabrication of electrospun scaffolds for the regeneration of tendons and ligaments, Materials 11 (2018) 1963, doi:10.3390/ma11101963.
[8] T. Chen, P. Zhang, J. Chen, Y. Hua, S. Chen, Long-term outcomes of anterior cruciate ligament reconstruction using either synthetics with remnant preservation or hamstring autografts: a 10-year longitudinal study, Am. J. Sports Med. 45 (2017) 2739–2750, doi:10.1177/0363546517721692.
[9] S. Liu, Y. Sun, F. Wan, Z. Ding, S. Chen, J. Chen, Advantages of an attached semitendinosus tendon graft in anterior cruciate ligament reconstruction in a rabbit model, Am. J. Sports Med. 46 (2018) 3227–3236, doi:10.1177/0363546518799357.
[10] M. Shafiq, Y. Jung, S.H. Kim, Insight on stem cell preconditioning and instructive biomaterials to enhance cell adhesion, retention, and engraftment for tissue repair, Biomaterials 90 (2016) 85–115, doi:10.1016/j.biomaterials.2016.03.020.
[11] A. Hoeben, B. Landuyt, M.S. Highley, H. Wildiers, A.T. Van Oosterom, E.A. De Bruijn, Vascular endothelial growth factor and angiogenesis, Pharmacol. Rev. 56 (2004) 549–580, doi:10.1124/pr.56.4.3.
[12] R.S. Apte, D.S. Chen, N. Ferrara, VEGF in signaling and disease: beyond discovery and development, Cell 176 (2019) 1248–1264, doi:10.1016/j.cell.2019.01.021.
[13] T. Yoshikawa, H. Tohyama, H. Enomoto, H. Matsumoto, Y. Toyama, K. Yasuda, Expression of vascular endothelial growth factor and angiogenesis in patellar tendon grafts in the early phase after anterior cruciate ligament reconstruction, Knee Surg. Sports Traumatol. Arthrosc. 14 (2006) 804–810, doi:10.1007/s00167-006-0051-8.
[14] J.R. Chen, L. Yang, L. Guo, X.J. Duan, Sodium hyaluronate as a drug-release system for VEGF 165 improves graft revascularization in anterior cruciate ligament reconstruction in a rabbit model, Exp. Ther. Med. 4 (2012) 430–434, doi:10.3892/etm.2012.629.
[15] C. Ai, D. Sheng, J. Chen, J. Cai, S. Wang, J. Jiang, S. Chen, Surface modification of vascular endothelial growth factor-loaded silk fibroin to improve biological performance of ultra-high-molecular-weight polyethylene via promoting angiogenesis, Int. J. Nanomed. 12 (2017) 7737–7750, doi:10.2147/IJN.S148845.
[16] K.S. Masters, Covalent growth factor immobilization strategies for tissue repair and regeneration, Macromol. Biosci. 11 (2011) 1149–1163, doi:10.1002/mabi.201000505.
[17] F. Yongcong, T. Zhang, L. Liverani, A.R. Boccaccini, W. Sun, Novel biomimetic fiber incorporated scaffolds for tissue engineering, J. Biomed. Mater. Res. 107 (2019) 2694–2705, doi:10.1002/jbm.a.36773.
[18] J. Cabanas-Danés, J. Huskens, P. Jonkheijm, Chemical strategies for the presentation and delivery of growth factors, J. Mater. Chem. B 2 (2014) 2381–2394, doi:10.1039/c3tb20853b.
[19] Z.L. Chi, A. Adini, A.E. Birsner, L. Bazinet, J.D. Akula, R.J. D'Amato, PR1P ameliorates neurodegeneration through activation of VEGF signaling pathway and remodeling of the extracellular environment, Neuropharmacology 148 (2019) 96–106, doi:10.1016/j.neuropharm.2018.12.029.
[20] A. Adini, H. Wu, D.T. Dao, V.H. Ko, L.J. Yu, A. Pan, M. Puder, S.Z. Mitiku, R. Potla, H. Chen, J.M. Rice, B.D. Matthews, PR1P stabilizes VEGF and upregulates its signaling to reduce elastase-induced murine emphysema, Am. J. Respir. Cell Mol. Biol. 63 (2020) 452–463, doi:10.1165/rcmb.2019-0434OC.
[21] A. Adini, I. Adini, Z. long Chi, R. Derda, A.E. Birsner, B.D. Matthews, R.J. D'Amato, A novel strategy to enhance angiogenesis in vivo using the small VEGF-binding peptide PR1P, Angiogenesis 20 (2017) 399–408, doi:10.1007/s10456-017-9556-7.
[22] Y. Cheng, Z. Chen, T. Liao, C. Lin, H.C. Shen, Y. Wang, C. Chang, R. Liu, R.P. Chen, P. Tu, An intranasally delivered peptide drug ameliorates cognitive decline in Alzheimer transgenic mice, EMBO Mol. Med. 9 (2017) 703–715, doi:10.15252/emmm.201606666.
[23] A.A. Galoyan, J.S. Sarkissian, V.A. Chavushyan, I.B. Meliksetyan, Z.E. Avagyan, M.V. Poghosyan, H.G. Vahradyan, H.H. Mkrtchian, D.O. Abrahamyan, Neuroprotection by hypothalamic peptide proline-rich peptide-1 in Aβ25-35 model of Alzheimer's disease, Alzheimer's Dementia 4 (2008) 332–344, doi:10.1016/j.jalz.2007.10.019.
[24] J. Crispim, H.A.M. Fernandes, S.C. Fu, Y.W. Lee, P. Jonkheijm, D.B.F. Saris, TGF-β1 activation in human hamstring cells through growth factor binding peptides on polycaprolactone surfaces, Acta Biomater. 53 (2017) 165–178, doi:10.1016/j.actbio.2017.01.066.
[25] M. Shafiq, O. Ali, S-B. Han, D-W. Kim, Mechanobiological strategies to enhance stem cell functionality for regenerative medicine and tissue engineering, Front. Cell Dev. Biol. (2021), doi:10.3389/fcell.2021.747398.
[26] Y. Chen, M. Shafiq, M. Liu, Y. Morsi, X. Mo, Advanced fabrication for electrospun three-dimensional nanofiber aerogels and scaffolds, Bioact. Mater. 5 (2020) 963–979, doi:10.1016/j.bioactmat.2020.06.023.
[27] X. Wang, J. Zhu, B. Sun, Q. Jin, H. Li, C. Xia, H. Wang, X. Mo, J. Wu, Harnessing electrospun nanofibers to recapitulate hierarchical fibrous structures of meniscus, J. Biomed. Mater. Res.-Part B 109 (2021) 201–213, doi:10.1002/jbm.b.34692.
[28] M. Tanzifi, M. Tavakkoli Yaraki, Z. Beiramzadeh, L. Heidarpoor Saremi, M. Najafifard, H. Moradi, M. Mansouri, M. Karami, H. Bazgir, Carboxymethyl cellulose improved adsorption capacity of polypyrrole/CMC composite nanoparticles for removal of reactive dyes: experimental optimization and DFT calculation, Chemosphere 255 (2020) 127052, doi:10.1016/j.chemosphere.2020.127052.
[29] D. Peng, S. Cheng, H. Li, X. Guo, Effective multi-functional biosorbent derived from corn stalk pith for dyes and oils removal, Chemosphere 272 (2021) 129963, doi:10.1016/j.chemosphere.2021.129963.
[30] Y. Xu, J. Wu, H. Wang, H. Li, N. Di, L. Song, S. Li, D. Li, Y. Xiang, W. Liu, X. Mo, Q. Zhou, Fabrication of electrospun poly(l-Lactide-co-ε-Caprolactone)/collagen nanoyarn network as a novel, three-dimensional, macroporous, aligned scaffold for tendon tissue engineering, Tissue Eng. Part C 19 (2013) 925–936, doi:10.1089/ten.tec.2012.0328.
[31] I.R. Serra, R. Fradique, M.C.S. Vallejo, T.R. Correia, S.P. Miguel, I.J. Correia, Production and characterization of chitosan/gelatin/β-TCP scaffolds for improved bone tissue regeneration, Mater. Sci. Eng. C 55 (2015) 592–604, doi:10.1016/j.msec.2015.05.072.
[32] M. Cui, L. Liu, N. Guo, R. Su, F. Ma, Preparation, cell compatibility and degradability of collagen-modified poly(lactic acid), Molecules 20 (2015) 595–607, doi:10.3390/molecules20010595.
[33] A. Sensini, C. Gotti, J. Belcari, A. Zucchelli, M.L. Focarete, C. Gualandi, I. Todaro, A.P. Kao, G. Tozzi, L. Cristofolini, Morphologically bioinspired hierarchical nylon 6,6 electrospun assembly recreating the structure and performance

of tendons and ligaments, Med. Eng. Phys. 71 (2019) 79–90, doi:10.1016/j.medengphy.2019.06.019.
[34] C. Gotti, A. Sensini, G. Fornaia, C. Gualandi, A. Zucchelli, M.L. Focarete, Biomimetic hierarchically arranged nanofibrous structures resembling the architecture and the passive mechanical properties of skeletal muscles: a step forward toward artificial muscle, Front. Bioeng. Biotechnol. 8 (2020) 767, doi:10.3389/fbioe.2020.00767.
[35] V.S. Rizi, F. Sharifianjazi, H. Jafarikhorami, N. Parvin, L.S Fard, M. Irani, A. Esmaeilkhanian, Sol–gel derived SnO2/Ag2O ceramic nanocomposite for H2 gas sensing applicati ons, Mater. Res. Exp. 6 (2019) 1150g2, doi:10.1088/2053-1591/ab511e.
[36] M. Kireš, Archimedes' principle in action, Phys. Educ. 42 (2007) 484–487, doi:10.1088/0031-9120/42/5/006.
[37] Q. Zeng, Y. Han, H. Li, J. Chang, Design of a thermosensitive bioglass/agarose-alginate composite hydrogel for chronic wound healing, J. Mater. Chem. B 3 (2015) 8856–8864, doi:10.1039/c5tb01758k.
[38] M. Shafiq, Y. Jung, S.H. Kim, In situ vascular regeneration using substance P-immobilised poly(L-Lactide-co-ε-caprolactone) scaffolds: Stem cell recruitment, angiogenesis, and tissue regeneration, Eur. Cell Mater. 30 (2015) 282–302, doi:10.22203/eCM.v030a20.
[39] B. Sun, T. Wu, J. Wang, D. Li, J. Wang, Q. Gao, M.A. Bhutto, H. El-Hamshary, S.S. Al-Deyab, X. Mo, Polypyrrole-coated poly(l-lactic acid-co-ϵ-caprolactone)/silk fibroin nanofibrous membranes promoting neural cell proliferation and differentiation with electrical stimulation, J. Mater. Chem. B 4 (2016) 6670–6679, doi:10.1039/c6tb01710j.
[40] Y. Chen, W. Xu, M. Shafiq, J. Tang, J. Hao, X. Xie, Z. Yuan, X. Xiao, Y. Liu, X. Mo, Three-dimensional porous gas-foamed electrospun nanofiber scaffold for cartilage regeneration, J. Colloid Interface Sci. 603 (2021) 94–109, doi:10.1016/j.jcis.2021.06.067.
[41] T.V. Chirila, Y. Hong, The vitreous humor, in: W. Murphy, J. Black, G. Hastings (Eds.), Handbook of Biomaterial Properties, Springer Nature Publishers, Switzerland, 2016, pp. 125–134, doi:10.1007/978-1-4939-3305-1_12.
[42] Z. Yuan, Y. Ren, M. Shafiq, Y. Chen, H. Tang, B. Li, M. EL-Newehy, H. EL-Hamshary, Y. Morsi, H. Zheng, X. Mo, Converging 3D printing and electrospinning: effect of poly(l-lactide)/gelatin based short nanofibers aerogels on tracheal regeneration, Macromol. Biosci. (2021) 2100342, doi:10.1002/mabi.202100342.
[43] M. Shafiq, S.H. Kim, Covalent immobilization of MSC-affinity peptide on poly(L-lactide-co-ε-caprolactone) copolymer to enhance stem cell adhesion and retention for tissue engineering applications, Macromol. Res. 24 (2016) 986–994, doi:10.1007/s13233-016-4138-x.
[44] J. Liu, M.Y. Xiu, J. Wu, H. Zhang, L. Yang, Y-C. Hu, B. Liu, Picrosirius-polarization method for collagen fiber detection in tendons: a mini-review, Orthop. Surg. 13 (2021) 701–707, doi:10.1111/os.12627.
[45] B. Han, I.A. Jones, Z. Yang, W. Fang, T. Vangsness, Repair of rotator cuff tendon defects in aged rats using a growth factor injectable gel scaffold, Athroscopy 36 (2020) 629–637, doi:10.1016/j.arthro.2019.09.015.
[46] N. Ferrara, A.P. Adamis, Ten years of anti-vascular endothelial growth factor therapy, Nat. Rev. Drug Discov. 15 (2016) 385–403, doi:10.1038/nrd.2015.17.
[47] N. Ferrara, Vascular endothelial growth factor: basic science and clinical progress, Endocrine Rev. 25 (2004) 581–611, doi:10.1210/er.2003-0027.
[48] H. Karvinen, E. Pasanen, T.T. Rissanen, P. Korpisalo, E. Vähäkangas, A. Jazwa, M. Giacca, S. Ylä-Herttuala, Long-term VEGF-A expression promotes aberrant angiogenesis and fibrosis in skeletal muscle, Gene Ther. 18 (2011) 1166–1172, doi:10.1038/gt.2011.66.
[49] R.J. Lee, M.L. Springer, W.E. Blanco-Bose, R. Shaw, P.C. Ursell, H.M. Blau, VEGF gene delivery to myocardium: Deleterious effects of unregulated expression, Circulation 102 (2000) 898–901, doi:10.1161/01.CIR.102.8.898.
[50] H. Huang, X. Zhang, X. Hu, Z. Shao, J. Zhu, L. Dai, Z. Man, L. Yuan, H. Chen, C. Zhou, Y. Ao, A functional biphasic biomaterial homing mesenchymal stem cells for in vivo cartilage regeneration, Biomaterials 35 (2014) 9608–9619, doi:10.1016/j.biomaterials.2014.08.020.
[51] Y. Xu, L. Duan, Y. Li, Y. She, J. Zhu, G. Zhou, G. Jiang, Y. Yang, Nanofibrillar decellularized wharton's jelly matrix for segmental tracheal repair, Adv. Funct. Mater. 30 (2020) 1910067, doi:10.1002/adfm.201910067.
[52] W.F. Mao, Y.F. Wu, Q.Q. Yang, Y.L. Zhou, X.T. Wang, P.Y. Liu, J.B. Tang, Modulation of digital flexor tendon healing by vascular endothelial growth factor gene transfection in a chicken model, Gene Ther. 24 (2017) 234–240, doi:10.1038/gt.2017.12.
[53] A. Adini, I. Adini, K. Ghosh, O. Benny, E. Pravda, R. Hu, D. Luyindula, R.J. D'Amato, The stem cell marker prominin-1/CD133 interacts with vascular endothelial growth factor and potentiates its action, Angiogenesis 16 (2013) 405–416, doi:10.1007/s10456-012-9323-8.
[54] M. Michaelides, M.C. Gaillard, P. Escher, L. Tiab, M. Bedell, F.X. Borruat, D. Barthelmes, R. Carmona, K. Zhang, E. White, M. McClements, A.G. Robson, G.E. Holder, K. Bradshaw, D.M. Hunt, A.R. Webster, A.T. Moore, D.F. Schorderet, F.L. Munier, The PROM1 mutation p.R373C causes an autosomal dominant bull's eye maculopathy associated with rod, rod-cone, and macular dystrophy, Investig. Ophthalmol. Vis. Sci. 51 (2010) 4771–4780, doi:10.1167/iovs.09-4561.
[55] Z. Yang, Y. Chen, C. Lillo, J. Chien, Z. Yu, M. Michaelides, M. Klein, K.A. Howes, Y. Li, Y. Kaminoh, H. Chen, C. Zhao, Y. Chen, Y.T. Al-Sheikh, G. Karan, D. Corbeil, P. Escher, S. Kamaya, C. Li, S. Johnson, J.M. Frederick, Y. Zhao, C. Wang, D.J. Cameron, W.B. Huttner, D.F. Schorderet, F.L. Munier, A.T. Moore, D.G. Birch, W. Baehr, D.M. Hunt, D.S. Williams, K. Zhang, Mutant prominin 1 found in patients with macular degeneration disrupts photoreceptor disk morphogenesis in mice, J. Clin. Invest. 119 (2009) 1396–1396, doi:10.1172/jci35891c1.
[56] F.E.-Z.E.-D. Yassin, R. El-Dawela, M. Kerim, Picrosirius red staining assessment of collagen after dermal roller application: A minimally invasive percutaneous collagen induction therapy, Indian J. Dermatopathol. Diagn. Dermatol. 1 (2014) 68–74, doi:10.4103/2349-6029.147289.
[57] R. Frangie, R.J. Warth, C.D. Harner, Editorial Commentary: Will suture tape augmentation prove to be the answer to anterior cruciate ligament graft remodeling, ultimate strength, and safe return to play? Arthroscopy 36 (2020) 490–491, doi:10.1016/j.arthro.2019.11.129.
[58] G. Nourissat, F. Berenbaum, D. Duprez, Tendon injury: From biology to tendon repair, Nat. Rev. Rheumatol. 11 (2015) 223–233, doi:10.1038/nrrheum.2015.26.